We are IntechOpen, the world's leading publisher of Open Access books
Built by scientists, for scientists

4,800
Open access books available

122,000
International authors and editors

135M
Downloads

154
Countries delivered to

Our authors are among the

TOP 1%
most cited scientists

12.2%
Contributors from top 500 universities

BOOK CITATION INDEX — CLARIVATE ANALYTICS — INDEXED

WEB OF SCIENCE™

Selection of our books indexed in the Book Citation Index
in Web of Science™ Core Collection (BKCI)

Interested in publishing with us?
Contact book.department@intechopen.com

Sliding-Mode Perturbation Observer-Based Sliding-Mode Control for VSC-HVDC Systems

Bo Yang, Tao Yu, Hongchun Shu and Pulin Cao

Additional information is available at the end of the chapter

Abstract

This chapter develops a sliding-mode perturbation observer-based sliding-mode control (POSMC) scheme for voltage source converter-based high voltage direct current (VSC-HVDC) systems. The combinatorial effect of nonlinearities, parameter uncertainties, unmodeled dynamics, and time-varying external disturbances is aggregated into a perturbation, which is estimated online by a sliding-mode state and perturbation observer (SMSPO). POSMC does not require an accurate VSC-HVDC system model and only the reactive power and DC voltage at the rectifier side while reactive and active powers at the inverter side need to be measured. Additionally, a considerable robustness can be provided through the real-time compensation of the perturbation, in which the upper bound of perturbation is replaced by the real-time estimation of the perturbation, such that the over-conservativeness of conventional sliding-mode control (SMC) can be effectively reduced. Four case studies are carried out on the VSC-HVDC system, such as active and reactive power tracking, AC bus fault, system parameter uncertainties, and weak AC gird connection. Simulation results verify its advantages over vector control and feedback linearization sliding-mode control. Then, a dSPACE-based hardware-in-the-loop (HIL) test is undertaken to validate the implementation feasibility of the proposed approach.

Keywords: sliding-mode control, sliding-mode perturbation observer, VSC-HVDC systems, HIL test

1. Introduction

In the past decades, the ever-increasing penetration of renewable energy (wind, solar, wave, hydro, and biomass) requires an extraordinarily reliable and effective transmission of electrical power from these new sources to the main power grid [1], in which hydropower has already

been fully exploited in many grids, such that a sustainable development can be achieved in future [2]. The problems and perspectives of converting present energy systems (mainly thermal and nuclear) into a 100% renewable energy system have been discussed with a conclusion that such idea is possible, which, however, raises that advanced transmission technologies are needed to realize this goal [3].

The need for more secure power grids and ever-increasing environmental concerns continue to drive the worldwide deployment of high voltage direct current (HVDC) transmission technology, which enables a more reliable and stable asynchronous interconnection of power networks that operate on different frequencies [4]. HVDC systems use power electronic devices to convert alternative current (AC) into direct current (DC), they are an economical way of transmitting bulk electrical power in DC over long distance overhead line or short submarine cable, while advanced extruded DC cable technologies have been used to increase power transmissions by at least 50%, which is also an important onshore solution. HVDC enables secure and stable asynchronous interconnection of power networks that operate on different frequencies. Different technologies have been used to design two-terminal HVDC systems for the purpose of a point-to-point power transfer, such as line-commutated converter (LCC)-based HVDC (LCC-HVDC) systems using grid-controlled mercury-arc valves or thyristors, capacitor-commutated converter (CCC)-based HVDC (CCC-HVDC) systems, or controlled series commutated converter (CSCC)-based HVDC (CSCC-HVDC) systems [5].

Voltage source converter-based high voltage direct current (VSC-HVDC) systems using insulated gate bipolar transistor (IGBT) technology have attracted increasing attentions due to the interconnection between the mainland and offshore wind farms, power flow regulation in alternating current (AC) power systems, long distance transmission [6], and introduction of the supergrid, which is a large-scale power grid interconnected between national power grids [7]. The main feature of the VSC-HVDC system is that no external voltage source is needed for communication, while active and reactive powers at each AC grid can be independently controlled [8, 9].

Traditionally, control of the VSC-HVDC system utilizes a nested-loop d-q vector control (VC) approach based on linear proportional-integral (PI) methods [10], whose control performance may be degraded with the change of operation conditions as its control parameters are tuned from one-point linearization model [11]. As VSC-HVDC systems are highly nonlinear resulting from converters and also operate in power systems with modeling uncertainties, many advanced control approaches are developed to provide a consistent control performance under various operation conditions, such as feedback linearization control (FLC) [12], which fully compensated the nonlinearities with the requirement of an accurate system model. Linear matrix inequality (LMI)-based robust control was developed in [13] to maximize the size of the uncertainty region within which closed-loop stability is maintained. In addition, adaptive backstepping control was designed to estimate the uncertain parameters by [14]. In [8, 9], power-synchronization control was employed to greatly increase the short-circuit capacity to the AC system. However, the aforementioned methods may not be adequate to simultaneously handle perturbations such as modeling uncertainties and time-varying external disturbances.

Based on the variable structure control strategy, sliding-mode control (SMC) is an effective and high-frequency switching control for nonlinear systems with modeling uncertainties and time-varying external disturbances. The main idea of SMC is to maintain the system sliding on a surface

in the state space via an appropriate switching logic; it features the simple implementation, disturbance rejection, fast response, and strong robustness [15]. While the malignant effect of chattering phenomenon can be reduced by predictive variable structure [16] and self-tuning sliding mode [17], SMC has been applied on electrical vehicles [18], power converters [19], induction machines [20], wind turbines [21], etc. Moreover, a feedback linearization sliding-mode control (FLSMC) has been developed for the VSC-HVDC system to offer invariant stability to modeling uncertainties by [22]. Basically, SMC assumes perturbations to be bounded and the prior knowledge of these upper bounds is required. However, it may be difficult or sometimes impossible to obtain these upper bounds, thus the supreme upper bound is chosen to cover the whole range of perturbations. As a consequence, SMC based on this knowledge becomes over-conservative which may cause a poor tracking performance and undesirable control oscillations [23].

During the past decades, several elegant approaches based on observers have been proposed to estimate perturbations, including the unknown input observer (UIO) [24], the disturbance observer (DOB) [25], the equivalent input disturbance (EID)-based estimation [26], enhanced decentralized PI control via advanced disturbance observer [27], the extended state observer (ESO)-based active disturbance rejection control (ADRC) [28], and practical multivariable control based on inverted decoupling and decentralized ADRC [29]. Among the above listed approaches, ESO requires the least amount of system information, in fact, only the system order needs to be known [30]. Due to such promising features, ESO-based control schemes have become more and more popular. Recently, ESO-based SMC has been developed to remedy the over-conservativeness of SMC via an online perturbation estimation. It observes both system states and perturbations by defining an extended state to represent the lumped perturbation, which can be then compensated online to improve the performance of system. Related applications can be referred to mechanical systems [31], missile systems [32], spherical robots [33], and DC-DC buck power converters [34].

This chapter uses an ESO called sliding-mode state and perturbation observer (SMSPO) [35, 36] to estimate the combinatorial effect of nonlinearities, parameter uncertainties, unmodeled dynamics, and time-varying external disturbances existed in VSC-HVDC systems, which is then compensated by the perturbation observer-based sliding-mode control (POSMC). The motivation to use POSMC, in this chapter, rather than SMC and our previous work [35–37] can be summarized as follows:

- The robustness of POSMC to the perturbation mostly depends on the perturbation compensation, while the ground of the robustness in SMC [18–22] is the discrete switching input. Furthermore, the upper bound of perturbation is replaced by the smaller bound of its estimation error, thus an over-conservative control input is avoided and the tracking accuracy is improved.

- POSMC can provide greater robustness than that of nonlinear adaptive control (NAC) [35, 36] and perturbation observer-based adaptive passive control (POAPC) [37] due to its inherent property of disturbance rejection.

Compared to VC [11], POSMC can provide a consistent control performance under various operation condition of the VSC-HVDC system and improve the power tracking by eliminating the power overshoot. Compared to FLSMC [22], POSMC only requires the measurement of

active and reactive power and DC voltage, which can provide a significant robustness and avoid an over-conservative control input as the real perturbation is estimated and compensated online. Four case studies are carried out to evaluate the control performance of POSMC through simulation, such as active and reactive power tracking, AC bus fault, system parameter uncertainties, and weak AC gird connection. Compared to the author's previous work on SMSPO [35, 36], a dSPACE simulator-based hardware-in-the-loop (HIL) test is undertaken to validate its implementation feasibility.

The rest of the chapter is organized as follows. In Section 2, the model of the two-terminal VSC-HVDC system is presented. In Section 3, POSMC design for the VSC-HVDC system is developed and discussed. Sections 4 and 5 present the simulation and HIL results, respectively. Finally, conclusions are drawn in Section 6.

2. VSC-HVDC system modeling

There are two VSCs in the VSC-HVDC system shown in **Figure 1**, in which the rectifier regulates the DC voltage and reactive power, while the inverter regulates the active and reactive power. Only the balanced condition is considered, e.g., the three phases have identical parameters and their voltages and currents have the same amplitude while each phase shifts 120° between themselves. The rectifier dynamics can be written at the angular frequency ω as [14].

$$\begin{cases} \dfrac{di_{d1}}{dt} = -\dfrac{R_1}{L_1}i_{d1} + \omega i_{q1} + u_{d1} \\ \dfrac{di_{q1}}{dt} = -\dfrac{R_1}{L_1}i_{q1} - \omega i_{d1} + u_{q1} \\ \dfrac{dV_{dc1}}{dt} = \dfrac{3u_{sq1}i_{q1}}{2C_1 V_{dc1}} - \dfrac{i_L}{C_1} \end{cases} \tag{1}$$

where the rectifier is connected with the AC grid via the equivalent resistance and inductance R_1 and L_1, respectively. C_1 is the DC bus capacitor, $u_{d1} = \frac{u_{sd1} - u_{rd}}{L_1}$ and $u_{q1} = \frac{u_{sq1} - u_{rq}}{L_1}$.

The inverter dynamics is written as

$$\begin{cases} \dfrac{di_{d2}}{dt} = -\dfrac{R_2}{L_2}i_{d2} + \omega i_{q2} + u_{d2} \\ \dfrac{di_{q2}}{dt} = -\dfrac{R_2}{L_2}i_{q2} - \omega i_{d2} + u_{q2} \\ \dfrac{dV_{dc2}}{dt} = \dfrac{3u_{sq2}i_{q2}}{2C_2 V_{dc2}} + \dfrac{i_L}{C_2} \end{cases} \tag{2}$$

where the inverter is connected with the AC grid via the equivalent resistance and inductance R_2 and L_2, respectively. C_2 is the DC bus capacitor, $u_{d2} = \frac{u_{sd2} - u_{id}}{L_2}$ and $u_{q2} = \frac{u_{sq2} - u_{iq}}{L_2}$.

The interconnection between the rectifier and inverter through DC cable is given as
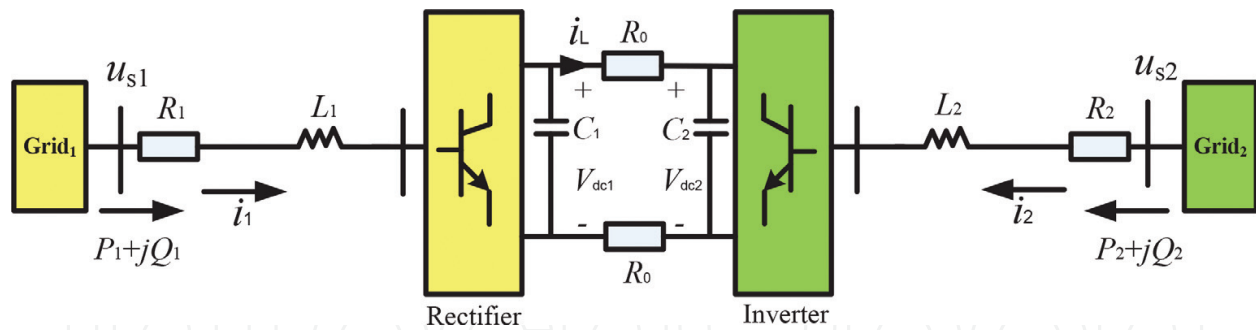
Figure 1. A standard two-terminal VSC-HVDC system.

$$V_{dc1}i_L = V_{dc2}i_L + 2R_0i_L^2 \tag{3}$$

where R_0 represents the equivalent DC cable resistance.

The phase-locked loop (PLL) [38] is used during the transformation of the *abc* frame to the *dq* frame. In the synchronous frame, u_{sd1}, u_{sd2}, u_{sq1}, and u_{sq2} are the *d*, *q* axes components of the respective AC grid voltages; i_{d1}, i_{d2}, i_{q1}, and i_{q2} are that of the line currents; u_{rd}, u_{id}, u_{rq}, and u_{iq} are that of the converter input voltages. P_1, P_2, Q_1, and Q_2 are the active and reactive powers transmitted from the AC grid to the VSC; V_{dc1} and V_{dc2} are the DC voltages; and i_L is the DC cable current.

At the rectifier side, the *q*-axis is set to be in phase with the AC grid voltage u_{s1}. Correspondingly, the *q*-axis is set to be in phase of the AC grid voltage u_{s2} at the inverter side. Hence, u_{sd1} and u_{sd2} are equal to 0, while u_{sq1} and u_{sq2} are equal to the magnitude of u_{s1} and u_{s2}. Note that this chapter adopts such framework from [12, 14, 22] to provide a consistent control design procedure and an easy control performance comparison, other framework can also be used as shown in [8, 9, 11]. The only difference of these two alternatives is the derived system equations, while the control design is totally the same. In addition, it is assumed that the VSC-HVDC system is connected to sufficiently strong AC grids, such that the AC grid voltage remains as an ideal constant. The power flows from the AC grid can be given as

$$\begin{cases} P_1 = \dfrac{3}{2}\left(u_{sq1}i_{q1} + u_{sd1}i_{d1}\right) = \dfrac{3}{2}u_{sq1}i_{q1} \\[2mm] Q_1 = \dfrac{3}{2}\left(u_{sq1}i_{d1} - u_{sd1}i_{q1}\right) = \dfrac{3}{2}u_{sq1}i_{d1} \\[2mm] P_2 = \dfrac{3}{2}\left(u_{sq2}i_{q2} + u_{sd2}i_{d2}\right) = \dfrac{3}{2}u_{sq2}i_{q2} \\[2mm] Q_2 = \dfrac{3}{2}\left(u_{sq2}i_{d2} - u_{sd2}i_{q2}\right) = \dfrac{3}{2}u_{sq2}i_{d2} \end{cases} \tag{4}$$

3. POSMC design for the VSC-HVDC system

3.1. Perturbation observer-based sliding-mode control

Consider an uncertain nonlinear system which has the following canonical form:

$$\begin{cases} \dot{x} = Ax + B(a(x) + b(x)u + d(t)) \\ y = x_1 \end{cases} \tag{5}$$

where $x = [x_1, x_2, \cdots, x_n]^{\mathrm{T}} \in \mathbb{R}^n$ is the state variable vector, $u \in \mathbb{R}$ and $y \in \mathbb{R}$ are the control input and system output, respectively. $a(x): \mathbb{R}^n \mapsto \mathbb{R}$ and $b(x): \mathbb{R}^n \mapsto \mathbb{R}$ are unknown smooth functions, and $d(t): \mathbb{R}^+ \mapsto \mathbb{R}$ represents the time-varying external disturbance. The $n \times n$ matrix A and the $n \times 1$ matrix B are of the canonical form as follows:

$$A = \begin{bmatrix} 0 & 1 & 0 & \cdots & 0 \\ 0 & 0 & 1 & \cdots & 0 \\ \vdots & & & & \vdots \\ 0 & 0 & 0 & \cdots & 1 \\ 0 & 0 & 0 & \cdots & 0 \end{bmatrix}_{n \times n}, \quad B = \begin{bmatrix} 0 \\ 0 \\ \vdots \\ 0 \\ 1 \end{bmatrix}_{n \times 1} \tag{6}$$

The perturbation of system (5) is defined as [35–37]

$$\Psi(x, u, t) = a(x) + (b(x) - b_0)u + d(t) \tag{7}$$

From the original system (5), the last state x_n can be rewritten in the presence of perturbation (6) as follows:

$$\dot{x}_n = a(x) + (b(x) - b_0)u + d(t) + b_0 u = \Psi(x, u, t) + b_0 u \tag{8}$$

Define a *fictitious state* $x_{n+1} = \Psi(x, u, t)$. Then, system (5) can be extended as

$$\begin{cases} y = x_1 \\ \dot{x}_1 = x_2 \\ \vdots \\ \dot{x}_n = x_{n+1} + b_0 u \\ \dot{x}_{n+1} = \dot{\Psi}(\cdot) \end{cases} \tag{9}$$

The new state vector becomes $x_e = [x_1, x_2, \cdots, x_n, x_{n+1}]^{\mathrm{T}}$, and following assumptions are made [35]:

- **A.1** b_0 is chosen to satisfy: $|b(x)/b_0 - 1| \leq \theta < 1$, where θ is a positive constant.

- **A.2** The functions $\Psi(x, u, t): \mathbb{R}^n \times \mathbb{R} \times \mathbb{R}^+ \mapsto \mathbb{R}$ and $\dot{\Psi}(x, u, t): \mathbb{R}^n \times \mathbb{R} \times \mathbb{R}^+ \mapsto \mathbb{R}$ are bounded over the domain of interest: $|\Psi(x, u, t)| \leq \gamma_1$, $|\dot{\Psi}(x, u, t)| \leq \gamma_2$ with $\Psi(0, 0, 0) = 0$ and $\dot{\Psi}(0, 0, 0) = 0$, where γ_1 and γ_2 are positive constants.

- **A.3** The desired trajectory y_d and its up to nth-order derivative are continuous and bounded.

The above three assumptions ensure the effectiveness of such perturbation estimation-based approach. In particular, assumptions A.1 and A.2 guarantee the closed-loop system

stability with perturbation estimation, while assumption A.3 ensures POSMC can drive the system state x to track a desired state $x_d = \left[y_d, y_d^{(1)}, \cdots, y_d^{(n-1)}\right]^{\mathrm{T}}$ [39]. In the consideration of the worst case, e.g., $y = x_1$ is the only measurable state, an $(n+1)$th-order SMSPO [35, 36] for the extended system (8) is designed to estimate the system states and perturbation, shown as follows:

$$
\begin{cases}
\dot{\hat{x}}_1 = \hat{x}_2 + \alpha_1 \tilde{x}_1 + k_1 \mathrm{sat}(\tilde{x}_1) \\
\quad\vdots \\
\dot{\hat{x}}_n = \widehat{\Psi}(\cdot) + \alpha_n \tilde{x}_1 + k_n \mathrm{sat}(\tilde{x}_1) + b_0 u \\
\dot{\widehat{\Psi}}(\cdot) = \alpha_{n+1} \tilde{x}_1 + k_{n+1} \mathrm{sat}(\tilde{x}_1)
\end{cases}
\tag{10}
$$

where $\tilde{x}_1 = x_1 - \hat{x}_1$, k_i and α_i, $i = 1, 2, \cdots, n + 1$, are positive coefficients, function $\mathrm{sat}(\tilde{x}_1)$ is defined as $\mathrm{sat}(\tilde{x}_1) = \tilde{x}_1/|\tilde{x}_1|$ when $|\tilde{x}_1| > \epsilon$ and $\mathrm{sat}(\tilde{x}_1) = \tilde{x}_1/\epsilon$ when $|\tilde{x}_1| \leq \epsilon$. The effect and setting of the SMSPO parameters are provided as follows:

- **The Luenberger observer constants** α_i, which are chosen to place the observer poles at the desired locations in the open left-half complex plane. In other words, α_i are chosen such that the root of $s^{n+1} + \alpha_1 s^n + \alpha_2 s^{n-1} + \cdots + \alpha_{n+1} = (s + \lambda_\alpha)^{n+1} = 0$ is in the open left-half complex plane. A larger value of α_i not only will accelerate the estimation rate of SMSPO, but also will result in a more significant effect of peaking phenomenon. Thus, a trade-off between the estimation rate and effect of peaking phenomenon must be made through trial-and-error. Normally, they are set to be much larger than the root of the closed-loop system to ensure a fast online estimation [37].

- **The sliding surface constants** k_i. $k_1 \geq |\tilde{x}_2|_{\max}$ must be chosen to guarantee the estimation error of SMSPO (9) will enter into the sliding surface $S_{\mathrm{spo}}(\tilde{x}) = \tilde{x}_1 = 0$ at $t > t_s$ and thereafter remain $S_{\mathrm{spo}} = 0$, $t \geq t_s$ [35, 39]. While the poles of the sliding surface λ_k are determined by choosing the ratio $k_i/k_1 (i = 2, 3, \cdots, n + 1)$ to put the root of $p^n + (k_2/k_1)p^{n-1} + \cdots + (k_n/k_1)p + (k_{n+1}/k_1) = (p + \lambda_k)^n = 0$ to be in the open left-half complex plane. Under Assumption A.2, SMSPO converges to a neighborhood of the origin if gains k_i are properly selected, which has been proved in [35, 40]. For a given k_1, a larger k_i not only will accelerate the estimation rate of SMSPO, but also will result in a degraded observer stability. Thus, a trade-off between the estimation rate and observer stability must be made through trial-and-error [39].

- **The layer thickness constant of saturation function** ϵ, which is a positive small scaler to replace the sign function by the saturation function, such that the chattering effect can be reduced. A larger ϵ will result in a smoother chattering, but a larger steady-state estimation error. Consequently, a trade-off between the chattering effect and steady-state estimation error must be made through trial-and-error. In practice, a value closes to 0 is recommended.

Moreover, the reduced estimation error dynamics on the sliding mode can be written as [35]

$$
\begin{cases}
\dot{\tilde{x}}_2 = -\dfrac{k_2}{k_1}\tilde{x}_2 + \tilde{x}_3 \\[2mm]
\dot{\tilde{x}}_3 = -\dfrac{k_3}{k_1}\tilde{x}_2 + \tilde{x}_4 \\[2mm]
\qquad\vdots \\[2mm]
\dot{\tilde{x}}_n = -\dfrac{k_n}{k_1}\tilde{x}_2 + \tilde{\Psi}(\cdot) \\[2mm]
\dot{\tilde{\Psi}}(\cdot) = -\dfrac{k_{n+1}}{k_1}\tilde{x}_2 + \dot{\Psi}(\cdot)
\end{cases}
\tag{11}
$$

Lemma 1 [39]. Consider extended system (8), design an SMSPO (9). If assumption A.2 holds for some value γ_2, then given any constant δ, the gains k_i can be chosen such that, from an initial estimation error $\tilde{x}_e(0)$, the estimation error $\tilde{x}_e$ converges exponentially into the neighborhood

$$
\|\tilde{x}_e\| \leq \delta
\tag{12}
$$

In particular,

$$
|\tilde{x}_i| \leq \frac{\delta}{\lambda_k^{n+1-i}}, \quad i = 2, \cdots, n+1, \quad \forall t > t_1.
\tag{13}
$$

where t_1 is the time constant which definition can be found in [39].

Remark 1. When SMSPO is used to estimate the perturbation, the upper bound of the derivative of perturbation γ_2 is required to guarantee the estimation accuracy, and such upper bound will result in a conservative observer gain. However, the conservative gain is only included in the observer loop, not in the controller loop.

Define an estimated sliding surface as

$$
\widehat{S}(x,t) = \sum_{i=1}^{n} \rho_i \left(\widehat{x}_i - y_d^{(i-1)} \right)
\tag{14}
$$

where the estimated sliding surface gains $\rho_i = C_{n-1}^{i-1}\lambda_c^{n-i}$, $i = 1, \cdots, n$, place all poles of the estimated sliding surface at $-\lambda_c$, where $\lambda_c > 0$.

Besides, the actual sliding surface is written by

$$
S = \sum_{i=1}^{n} \rho_i \left(x_i - y_d^{(i-1)} \right)
\tag{15}
$$

Hence, the estimation error of the sliding surface can be directly calculated as

$$
\tilde{S} = S - \widehat{S} = \sum_{i=1}^{n} \rho_i \tilde{x}_i
\tag{16}
$$

Construct a Lyapunov function as follows:

$$V = \frac{1}{2}\widehat{S}^2 \tag{17}$$

The attractiveness of sliding surface is achieved if $\dot{V} < 0$ for all $\tilde{x} \not\subseteq \widehat{S}$, that is, the control u needs to be designed to enforce $\widehat{S}\dot{\widehat{S}} < 0$ outside a prescribed manifold $|\widehat{S}| < \varepsilon_c$.

The POSMC for system (5) is designed as

$$u = \frac{1}{b_0}\left[y_d^{(n)} - \sum_{i=1}^{n-1}\rho_i\left(\widehat{x}_{i+1} - y_d^{(i)}\right) - \zeta\widehat{S} - \varphi\mathrm{sat}\left(\widehat{S}\right) - \widehat{\Psi}(\cdot) \right] \tag{18}$$

where ζ and φ are control gains which are chosen to fulfill the attractiveness of the estimated sliding surface $\widehat{S}$.

Differentiate estimated sliding surface (13) along SMSPO (9), use the reduced estimation error dynamics (10), it yields

$$\dot{\widehat{S}} = \widehat{\Psi}(\cdot) + b_0 u + \frac{k_n}{k_1}\tilde{x}_2 - y_d^{(n)} + \sum_{i=1}^{n-1}\rho_i\left(\widehat{x}_{i+1} - y_d^{(i)} + \frac{k_i}{k_1}\tilde{x}_2\right) \tag{19}$$

Substitute control (17) into the above Eq. (18), leads to

$$\dot{\widehat{S}} = \sum_{i=1}^{n}\rho_i\frac{k_i}{k_1}\tilde{x}_2 - \zeta\widehat{S} - \varphi\mathrm{sat}\left(\widehat{S}, \varepsilon_c\right) \tag{20}$$

Consequently, the attractiveness of sliding surface can be derived as

$$\zeta|\widehat{S}| + \varphi > \sum_{i=1}^{n}\rho_i\frac{k_i}{k_1}|\tilde{x}_2| \tag{21}$$

which will be fulfilled with the relationship of k_1 if

$$\zeta|\widehat{S}| + \varphi > k_1\sum_{i=1}^{n}\rho_i\frac{k_i}{k_1} \tag{22}$$

The above condition can be immediately satisfied if control gain φ is chosen as

$$\varphi > k_1\sum_{i=1}^{n}\rho_i\frac{k_i}{k_1} \tag{23}$$

which, using gains k_i, yields

$$\varphi > k_1\sum_{i=1}^{n}\rho_i C_n^{i-1}\lambda_k^{i-1} \tag{24}$$

This condition ensures the existence of a sliding mode on the boundary layer $|\widehat{S}| \le \varepsilon_c$. From system (15) one can easily calculate

$$\dot{\tilde{S}} = \sum_{i=1}^{n-1} \rho_i \tilde{x}_{i+1} - \sum_{i=1}^{n} \rho_i \frac{k_i}{k_1} \tilde{x}_2 + \tilde{\Psi}(\cdot) \tag{25}$$

As $\widehat{S} = S - \tilde{S}$, the actual S-dynamics of sliding surface can be obtained with dynamics (19) as

$$\dot{S} + \left(\zeta + \frac{\varphi}{\varepsilon_c} \right) S = \left(\zeta + \frac{\varphi}{\varepsilon_c} \right) \sum_{i=1}^{n} \rho_i \tilde{x}_i + \sum_{i=1}^{n-1} \rho_i \tilde{x}_{i+1} + \tilde{\Psi}(\cdot) \tag{26}$$

It is definite that the driving term of S-dynamics is the sum of the estimation errors of states and the perturbation. The bounds of the sliding surface can be calculated by

$$|\widehat{S}| \le \varepsilon_c \Rightarrow |S - \tilde{S}| \le \varepsilon_c \Rightarrow |S| \le |\tilde{S}| + \varepsilon_c \Rightarrow |S| \le \left| \sum_{i=1}^{n} \rho_i \tilde{x}_i \right| + \varepsilon_c \le \frac{\delta}{\lambda_k^{n+1}} \sum_{i=2}^{n} \rho_i \lambda_k^i + \varepsilon_c, \quad \forall t > t_1. \tag{27}$$

Based on bounds (26), together with the polynomial gains ρ_i, the states tracking error satisfies the following relationship [41]

$$|x^{(i)}(t) - x_d^{(i)}(t)| \le (2\lambda_c)^i \frac{\varepsilon_c}{\lambda_c^n} + \frac{\delta}{\lambda_k^{n+1}} \sum_{j=2}^{n} \left(\frac{\lambda_k}{\lambda_c} \right)^j C_{n-1}^j, \quad i = 0, 1, \cdots, n-1. \tag{28}$$

Note that POSMC does not require an accurate system model, and only one state measurement $y = x_1$ is needed. As the upper bound of perturbation $\Psi(\cdot)$ is replaced by the smaller bound of its estimation error $\tilde{\Psi}(\cdot)$, a smaller control gain is needed such that the over-conservativeness of SMC can be avoided [35].

Remark 2. The motivation to use SMSPO is due to the fact that the sliding-mode observer potentially offers advantages similar to those of sliding-mode controllers, in particular, inherent robustness to parameter uncertainty and external disturbances [42]. It is a high-performance state estimator with a simple structure and is well suited for uncertain nonlinear systems [31]. Moreover, it has the merits of simple structure and easy analysis of the closed-loop system stability compared to that of ADRC which uses a nonlinear observer [28], while they can provide almost the same performance of perturbation estimation.

The overall design procedure of POSMC for system (5) can be summarized as follows:

Step 1. Define perturbation (6) for the original nth-order system (5);

Step 2. Define a *fictitious state* $x_{n+1} = \Psi(\cdot)$ to represent perturbation (6);

Step 3. Extend the original nth-order system (5) into the extended $(n + 1)$th-order system (8);

Step 4. Design the $(n+1)$th-order SMSPO (9) for the extended $(n+1)$th-order system (8) to obtain the state estimate $\widehat{x}$ and the perturbation estimate $\widehat{\Psi}(\cdot)$ by the only measurement of x_1;

Step 5. Design controller (17) for the original nth-order system (5), in which the estimated sliding surface $\widehat{S}$ is calculated by (13).

3.2. Rectifier controller design

Choose the system output $y_r = [y_{r1}, y_{r2}]^T = [Q_1, V_{dc1}]^T$, let Q_1^* and V_{dc1}^* be the given references of the reactive power and DC voltage, respectively. Define the tracking error $e_r = [e_{r1}, e_{r2}]^T = [Q_1 - Q_1^*, V_{dc1} - V_{dc1}^*]^T$, differentiate e_r for rectifier (1) until the control input appears explicitly, yields

$$\begin{bmatrix} \dot{e}_{r1} \\ \ddot{e}_{r2} \end{bmatrix} = \begin{bmatrix} f_{r1} - \dot{Q}_1^* \\ f_{r2} - \ddot{V}_{dc1}^* \end{bmatrix} + B_r \begin{bmatrix} u_{d1} \\ u_{q1} \end{bmatrix} \tag{29}$$

where

$$\begin{cases} f_{r1} = \dfrac{3u_{sq1}}{2}\left(-\dfrac{R_1}{L_1}i_{d1} + \omega i_{q1}\right) \\[3mm] f_{r2} = \dfrac{3u_{sq1}}{2C_1 V_{dc1}}\left[-\omega i_{d1} - \dfrac{R_1}{L_1}i_{q1} - \dfrac{i_{q1}}{V_{dc1}}\left(\dfrac{3u_{sq1}i_{q1}}{2C_1 V_{dc1}} - \dfrac{i_L}{C_1}\right)\right] \\[3mm] \qquad - \dfrac{1}{2R_0 C_1}\left(\dfrac{3u_{sq1}i_{q1}}{2C_1 V_{dc1}} - \dfrac{i_L}{C_1} - \dfrac{3u_{sq2}i_{q2}}{2C_2 V_{dc2}} - \dfrac{i_L}{C_2}\right) \end{cases} \tag{30}$$

and

$$B_r = \begin{bmatrix} \dfrac{3u_{sq1}}{2L_1} & 0 \\[3mm] 0 & \dfrac{3u_{sq1}}{2C_1 L_1 V_{dc1}} \end{bmatrix} \tag{31}$$

The determinant of matrix B_r is obtained as $|B_r| = 9u_{sq1}^2/(4C_1 L_1^2 V_{dc1})$, which is nonzero within the operation range of the rectifier, thus system (28) is linearizable.

Assume all the nonlinearities are unknown, define the perturbations $\Psi_{r1}(\cdot)$ and $\Psi_{r2}(\cdot)$ as

$$\begin{bmatrix} \Psi_{r1}(\cdot) \\ \Psi_{r2}(\cdot) \end{bmatrix} = \begin{bmatrix} f_{r1} \\ f_{r2} \end{bmatrix} + (B_r - B_{r0})\begin{bmatrix} u_{d1} \\ u_{q1} \end{bmatrix} \tag{32}$$

where the constant control gain B_{r0} is given by

$$B_{r0} = \begin{bmatrix} b_{r10} & 0 \\ 0 & b_{r20} \end{bmatrix} \tag{33}$$

Then system (28) can be rewritten as

$$\begin{bmatrix} \dot{e}_{r1} \\ \ddot{e}_{r2} \end{bmatrix} = \begin{bmatrix} \Psi_{r1}(\cdot) \\ \Psi_{r2}(\cdot) \end{bmatrix} + B_{r0} \begin{bmatrix} u_{d1} \\ u_{q1} \end{bmatrix} - \begin{bmatrix} \dot{Q}_1^* \\ \ddot{V}_{dc1}^* \end{bmatrix} \tag{34}$$

Define $z'_{11} = Q_1$, a second-order sliding-mode perturbation observer (SMPO) is used to estimate $\Psi_{r1}(\cdot)$ as

$$\begin{cases} \dot{\hat{z}}'_{11} = \widehat{\Psi}_{r1}(\cdot) + \alpha'_{r1}\tilde{Q}_1 + k'_{r1}\text{sat}(\tilde{Q}_1) + b_{r10}u_{d1} \\ \dot{\widehat{\Psi}}_{r1}(\cdot) = \alpha'_{r2}\tilde{Q}_1 + k'_{r2}\text{sat}(\tilde{Q}_1) \end{cases} \tag{35}$$

where observer gains k'_{r1}, k'_{r2}, α'_{r1}, and α'_{r2} are all positive constants.

Define $z_{11} = V_{dc1}$ and $z_{12} = \dot{z}_{11}$, a third-order SMSPO is used to estimate $\Psi_{r2}(\cdot)$ as

$$\begin{cases} \dot{\hat{z}}_{11} = \hat{z}_{12} + \alpha_{r1}\tilde{V}_{dc1} + k_{r1}\text{sat}(\tilde{V}_{dc1}) \\ \dot{\hat{z}}_{12} = \widehat{\Psi}_{r2}(\cdot) + \alpha_{r2}\tilde{V}_{dc1} + k_{r2}\text{sat}(\tilde{V}_{dc1}) + b_{r20}u_{q1} \\ \dot{\widehat{\Psi}}_{r2}(\cdot) = \alpha_{r3}\tilde{V}_{dc1} + k_{r3}\text{sat}(\tilde{V}_{dc1}) \end{cases} \tag{36}$$

where observer gains k_{r1}, k_{r2}, k_{r3}, α_{r1}, α_{r2}, and α_{r3} are all positive constants.

The above observers (31) and (32) only need the measurement of reactive power Q_1 and DC voltage V_{dc1} at the rectifier side, which can be directly obtained in practice.

The estimated sliding surface of system (28) is defined as

$$\begin{bmatrix} \widehat{S}_{r1} \\ \widehat{S}_{r2} \end{bmatrix} = \begin{bmatrix} \hat{z}'_{11} - Q_1^* \\ \rho_1(\hat{z}_{11} - V_{dc1}^*) + \rho_2(\hat{z}_{12} - \dot{V}_{dc1}^*) \end{bmatrix} \tag{37}$$

where ρ_1 and ρ_2 are the positive sliding surface gains. The attractiveness of the estimated sliding surface (33) ensures reactive power Q_1 and DC voltage V_{dc1} can track to their reference.

The POSMC of system (28) is designed as

$$\begin{bmatrix} u_{d1} \\ u_{q1} \end{bmatrix} = B_{r0}^{-1} \begin{bmatrix} -\widehat{\Psi}_{r1}(\cdot) + \dot{Q}_1^* - \zeta'_r\widehat{S}_{r1} - \varphi'_r\text{sat}(\widehat{S}_{r1}) \\ -\widehat{\Psi}_{r2}(\cdot) + \ddot{V}_{dc1}^* - \rho_1(\hat{z}_{12} - \dot{V}_{dc1}^* - \zeta_r\widehat{S}_{r2} - \varphi_r\text{sat}(\widehat{S}_{r2}) \end{bmatrix} \tag{38}$$

where positive control gains ζ_r, ζ'_r, φ_r, ρ_1, and φ'_r are chosen to ensure the attractiveness of estimated sliding surface (33).

During the most severe disturbance, both the reactive power and DC voltage reduce from their initial value to around zero within a short period of time Δ. Thus, the boundary values of the system state and perturbation estimates can be obtained as $|\hat{z}'_{11}| \leq |Q_1^*|$, $|\widehat{\Psi}_{r1}(\cdot)| \leq |Q_1^*|/\Delta$, $|\hat{z}_{11}| \leq |V_{dc1}^*|$, $|\hat{z}_{12}| \leq |V_{dc1}^*|/\Delta$, and $|\widehat{\Psi}_{r2}(\cdot)| \leq |V_{dc1}^*|/\Delta^2$, respectively.

3.3. Inverter controller design

Choose the system output $y_i = [y_{i1}, y_{i2}]^T = [Q_2, P_2]^T$, let Q_2^* and P_2^* be the given references of the reactive and active power, respectively. Define the tracking error $e_i = [e_{i1}, e_{i2}]^T = [Q_2 - Q_2^*, P_2 - P_2^*]^T$, differentiate e_i for inverter (2) until the control input appears explicitly, yields

$$\begin{bmatrix} \dot{e}_{i1} \\ \dot{e}_{i2} \end{bmatrix} = \begin{bmatrix} f_{i1} - \dot{Q}_2^* \\ f_{i2} - \dot{P}_2^* \end{bmatrix} + B_i \begin{bmatrix} u_{d2} \\ u_{q2} \end{bmatrix} \tag{39}$$

where

$$\begin{cases} f_{i1} = \dfrac{3u_{sq2}}{2}\left(-\dfrac{R_2}{L_2} i_{d2} + \omega i_{q2} \right) \\[3mm] f_{i2} = \dfrac{3u_{sq2}}{2}\left(-\dfrac{R_2}{L_2} i_{q2} - \omega i_{d2} \right) \end{cases} \tag{40}$$

and

$$B_i = \begin{bmatrix} \dfrac{3u_{sq2}}{2L_2} & 0 \\[3mm] 0 & \dfrac{3u_{sq2}}{2L_2} \end{bmatrix} \tag{41}$$

The determinant of matrix B_i is obtained as $|B_i| = 9u_{s2}^2/(4L_2^2)$, which is nonzero within the operation range of the inverter, thus system (35) is linearizable.

Assume all the nonlinearities are unknown, define the perturbations $\Psi_{i1}(\cdot)$ and $\Psi_{i2}(\cdot)$ as

$$\begin{bmatrix} \Psi_{i1}(\cdot) \\ \Psi_{i2}(\cdot) \end{bmatrix} = \begin{bmatrix} f_{i1} \\ f_{i2} \end{bmatrix} + (B_i - B_{i0}) \begin{bmatrix} u_{d2} \\ u_{q2} \end{bmatrix} \tag{42}$$

where the constant control gain B_{i0} is given by

$$B_{i0} = \begin{bmatrix} b_{i10} & 0 \\ 0 & b_{i20} \end{bmatrix} \tag{43}$$

Then system (35) can be rewritten as

$$\begin{bmatrix} \dot{e}_{i1} \\ \dot{e}_{i2} \end{bmatrix} = \begin{bmatrix} \Psi_{i1}(\cdot) \\ \Psi_{i2}(\cdot) \end{bmatrix} + B_{i0} \begin{bmatrix} u_{d2} \\ u_{q2} \end{bmatrix} - \begin{bmatrix} \dot{Q}_2^* \\ \dot{P}_2^* \end{bmatrix} \tag{44}$$

Similarly, define $z_{21}' = Q_2$ and $z_{21} = P_2$, two second-order SMPOs are used to estimate $\Psi_{i1}(\cdot)$ and $\Psi_{i2}(\cdot)$, respectively, as

$$\begin{cases} \dot{\hat{z}}'_{21} = \widehat{\Psi}_{i1}(\cdot) + \alpha'_{i1}\tilde{Q}_2 + k'_{i1}\text{sat}(\tilde{Q}_2) + b_{i10}u_{d2} \\ \dot{\widehat{\Psi}}_{i1}(\cdot) = \alpha'_{i2}\tilde{Q}_2 + k'_{i2}\text{sat}(\tilde{Q}_2) \end{cases} \tag{45}$$

where observer gains k'_{i1}, k'_{i2}, α'_{i1}, and α'_{i2} are all positive constants.

$$\begin{cases} \dot{\hat{z}}_{21} = \widehat{\Psi}_{i2}(\cdot) + \alpha_{i1}\tilde{P}_2 + k_{i1}\text{sat}(\tilde{P}_2) + b_{i20}u_{q2} \\ \dot{\widehat{\Psi}}_{i2}(\cdot) = \alpha_{i2}\tilde{P}_2 + k_{i2}\text{sat}(\tilde{P}_2) \end{cases} \tag{46}$$

where observer gains k_{i1}, k_{i2}, α_{i1}, and α_{i2} are all positive constants.

The above observers (38) and (39) only need the measurement of reactive power Q_2 and active power P_2 at the inverter side, which can be directly obtained in practice.

The estimated sliding surface of system (35) is defined as

$$\begin{bmatrix} \widehat{S}_{i1} \\ \widehat{S}_{i2} \end{bmatrix} = \begin{bmatrix} \hat{z}'_{21} - Q^*_2 \\ \hat{z}_{21} - P^*_2 \end{bmatrix} \tag{47}$$

Similarly, the attractiveness of the estimated sliding surface (40) ensures the reactive power Q_2 and active power P_2 can track to their reference.

The POSMC of system (35) is designed as

$$\begin{bmatrix} u_{d2} \\ u_{q2} \end{bmatrix} = B_{i0}^{-1} \begin{bmatrix} -\widehat{\Psi}_{i1}(\cdot) + \dot{Q}^*_2 - \zeta'_i\widehat{S}_{i1} - \varphi'_i\text{sat}(\widehat{S}_{i1}) \\ -\widehat{\Psi}_{i2}(\cdot) + \dot{P}^*_2 - \zeta_i\widehat{S}_{i2} - \varphi_i\text{sat}(\widehat{S}_{i2}) \end{bmatrix} \tag{48}$$

where positive control gains ζ_i, ζ_i, φ_i, and φ'_i are chosen to ensure the attractiveness of estimated sliding surface (40).

Similarly, the boundary values of the system state and perturbation estimates can be obtained as $|\hat{z}'_{21}| \leq |Q^*_2|$, $|\widehat{\Psi}_{i1}(\cdot)| \leq |Q^*_2|/\Delta$, $|\hat{z}_{21}| \leq |P^*_2|$, and $|\widehat{\Psi}_{i2}(\cdot)| \leq |P^*_2|/\Delta$, respectively.

Note that control outputs (34) and (41) are modulated by the sinusoidal pulse width modulation (SPWM) technique [6] in this chapter. The overall controller structure of the VSC-HVDC system is illustrated by **Figure 2**, in which only reactive power Q_1 and DC voltage V_{dc1} need to be measured for rectifier controller (34), while active power P_2 and reactive power Q_2 for inverter controller (41).

Remark 3 The conventional linear PI/PID control scheme employs an inner current loop to regulate the current [11], which could employ a synchronous reference frame (SRF)-based current controller [43] to avoid overcurrent. In contrast, the proposed POSMC (34) and (41) actually contains no current in its control law, while it cannot handle the overcurrent. Hence, the overcurrent protection devices [44] will be activated to prevent the overcurrent to grow, which can be seen in **Figure 2**.
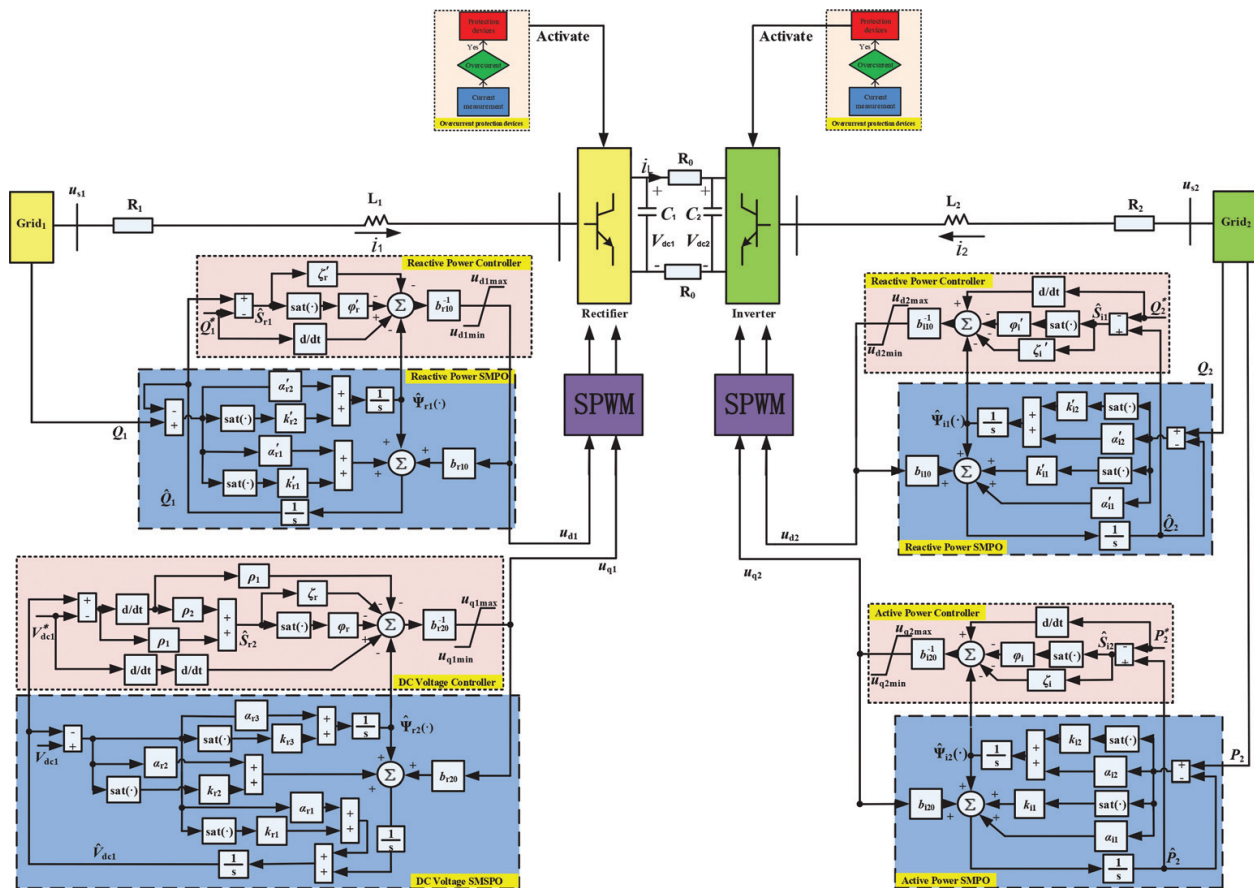
Figure 2. The overall controller structure of the VSC-HVDC system.

4. Simulation results

POSMC is applied on the VSC-HVDC system illustrated in **Figure 1**. The AC grid frequency is 50 Hz and VSC-HVDC system parameters are given in **Table 1**. POSMC parameters are provided in **Table 2**, in which the observer poles are allocated as $\lambda_{\alpha_r} = 100$ and $\lambda_{\alpha'_r} = \lambda_{\alpha_i} = \lambda_{\alpha'_i} = 20$,

AC system-based voltage	$V_{AC\ base}$	132 kV
DC cable base voltage	$V_{DC\ base}$	150 kV
System base power	S_{base}	100 MVA
AC system resistance (25 km)	R_1, R_2	0.05 Ω/km
AC system inductance (25 km)	L_1, L_2	0.026 mH/km
DC cable resistance (50 km)	R_0	0.21 Ω/km
DC bus capacitance	C_1, C_2	11.94 μF

Table 1. The VSC-HVDC system parameters.

Rectifier controller gains			
$b_{r10} = 100$	$b_{r20} = 7000$	$\rho_1 = 800$	$\rho_2 = 1$
$\zeta_r = 20$	$\zeta_r' = 10$	$\varphi_r = 20$	$\varphi_r' = 20$
Rectifier observer gains			
$\alpha_{r1} = 300$	$\alpha_{r1}' = 40$	$\alpha_{r2} = 3 \times 10^4$	$\alpha_{r2}' = 400$
$\alpha_{r3} = 10^6$	$\Delta = 0.01$	$\epsilon = 0.1$	$k_{r1} = 100$
$k_{r1}' = 75$	$k_{r2} = 10^5$	$k_{r2}' = 3.75 \times 10^4$	$k_{r3} = 2.5 \times 10^7$
Inverter controller gains			
$b_{i10} = 50$	$b_{i20} = 50$	$\zeta_i = 10$	$\zeta_i' = 10$
$\varphi_i = 10$	$\varphi_i' = 10$		
Inverter observer gains			
$\alpha_{i1} = 40$	$\alpha_{i1}' = 40$	$\alpha_{i2} = 400$	$\alpha_{i2}' = 400$
$k_{i1} = 75$	$k_{i1}' = 75$	$k_{i2} = 3.75 \times 10^4$	$k_{i2}' = 3.75 \times 10^4$

Table 2. POSMC parameters for the VSC-HVDC system.
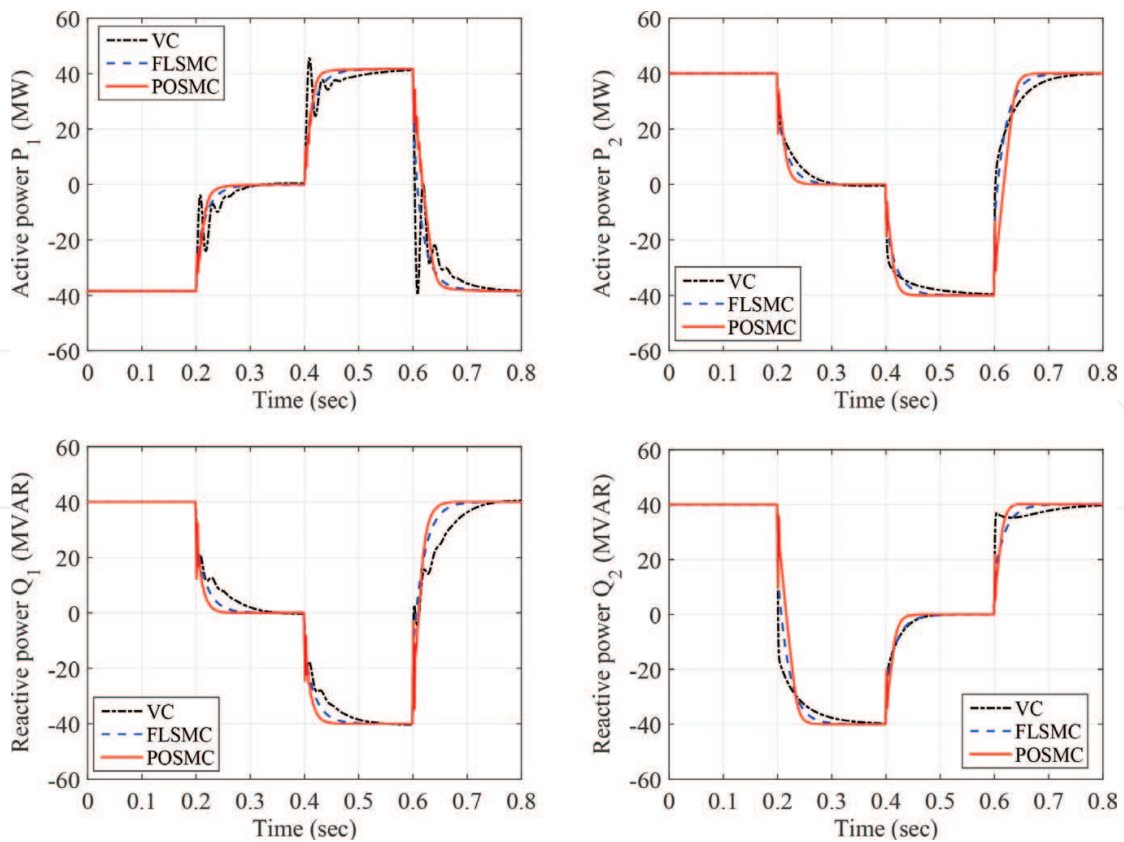
Figure 3. System responses obtained under the active and reactive power tracking.

while control inputs are bounded as $|u_{qi}| \leq 80$ kV and $|u_{di}| \leq 60$ kV, where $i = 1, 2$. The switching frequency is 1620 Hz for both rectifier and inverter, which is taken from [22]. The control performance of POSMC is compared to that of VC [11] and FLSMC [22] by the following four cases. In addition, two identical three-level neutral-point-clamped VSCs model for each rectifier and inverter from Matlab/Simulink SimPowerSystems are employed, which structure and parameters are taken directly from [11]. The simulation is executed on Matlab/Simulink 7.10 using a personal computer with an IntelR CoreTMi7 CPU at 2.2 GHz and 8 GB of RAM.

(1) Case 1: Active and reactive power tracking: The references of active and reactive power are set to be a series of step change occurs at $t = 0.2$ s, $t = 0.4$ s and restores to the original value at $t = 0.6$ s, while DC voltage is regulated at the rated value $V_{dc1}^* = 150$ kV. The system responses are illustrated by **Figure 3**. One can find that POSMC has the fastest tracking rate and maintains a consistent control performance under different operation conditions.

(2) Case 2: 5-cycle line-line-line-ground (LLLG) fault at AC bus 1: A five-cycle LLLG fault occurs at AC bus 1 when $t = 0.1$ s. Due to the fault, AC voltage at the corresponding bus is decreased to a critical level. **Figure 4** shows that POSMC can effectively restore the system with the smallest active power oscillations. Response of perturbation estimation is demonstrated in **Figure 5**, which shows that SMSPO and SMPO can estimate the perturbations with a fast tracking rate.
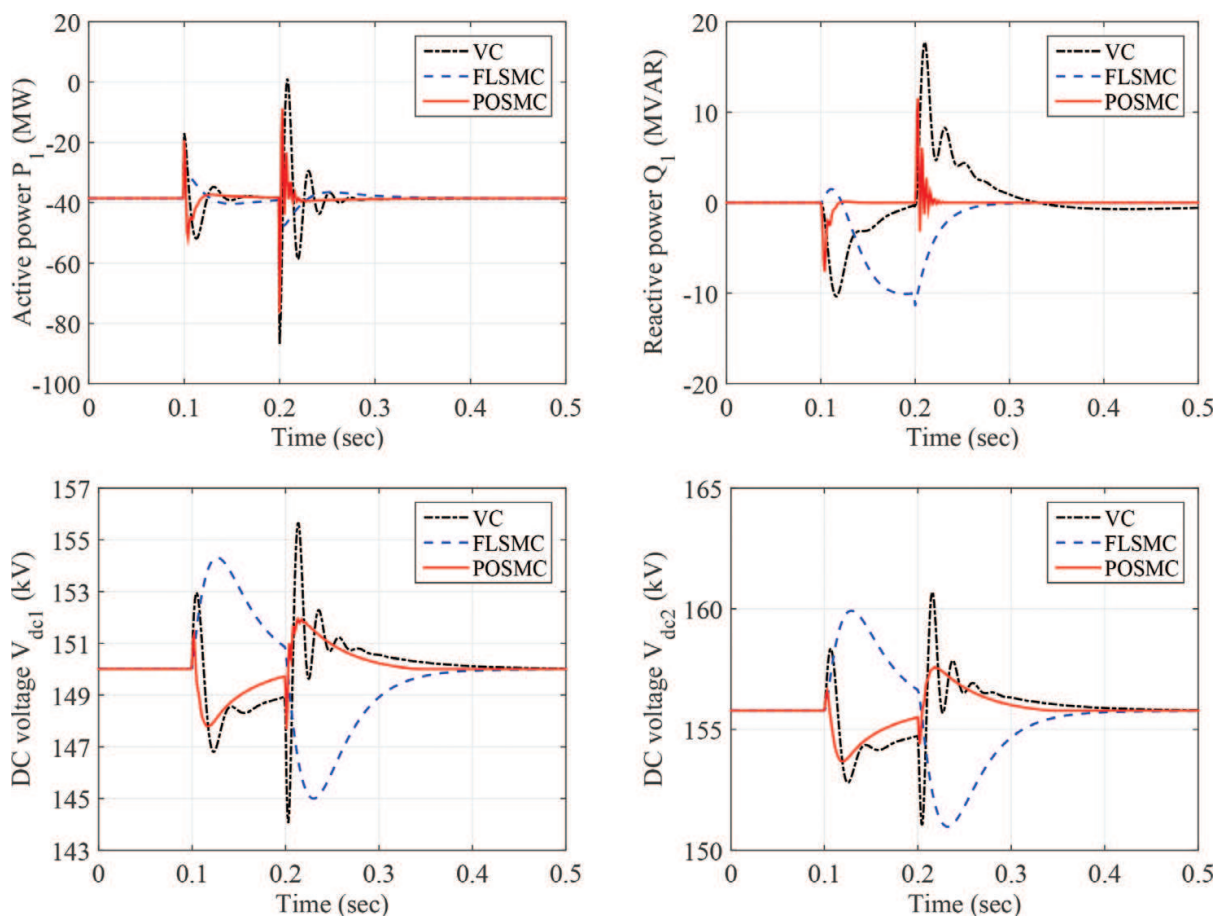

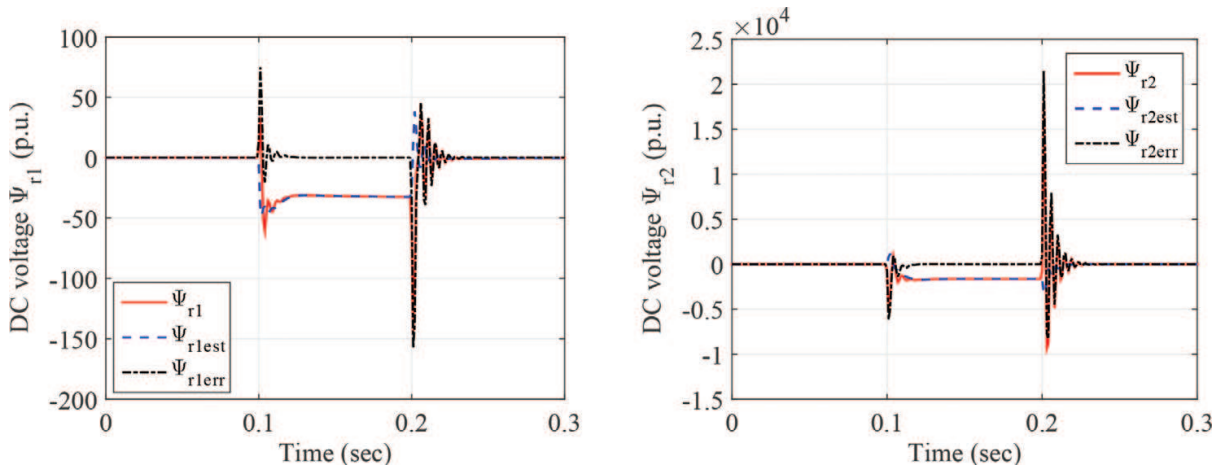**Figure 4.** System responses obtained under the five-cycle LLLG fault at AC bus 1.

Figure 5. Estimation errors of the perturbations obtained under the five-cycle LLLG fault at AC bus 1.

(3) Case 3: Weak AC grid connection: The AC grids are assumed to be sufficiently strong such that AC bus voltages are ideal constants. It is worth considering a weak AC grid connected to the rectifier, e.g., offshore wind farms, which voltage u_{s1} is no longer a constant but a time-varying function. A voltage fluctuation that occurs from 0.15 to 1.05 s caused by the wind speed variation is applied, which corresponds to $u_{s1} = 1 + 0.15\sin(0.2\pi t)$. System responses are presented in **Figure 6**, it illustrates that both DC voltage and reactive power are oscillatory,
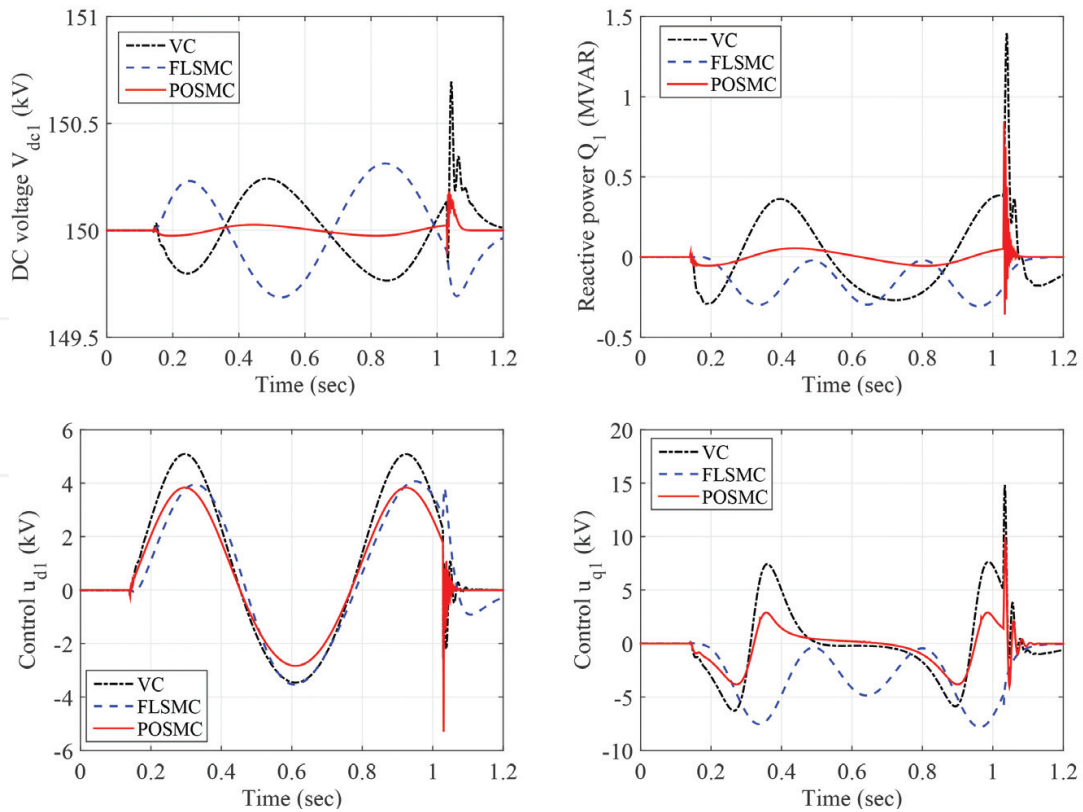
Figure 6. System responses obtained with the weak AC grid connection.
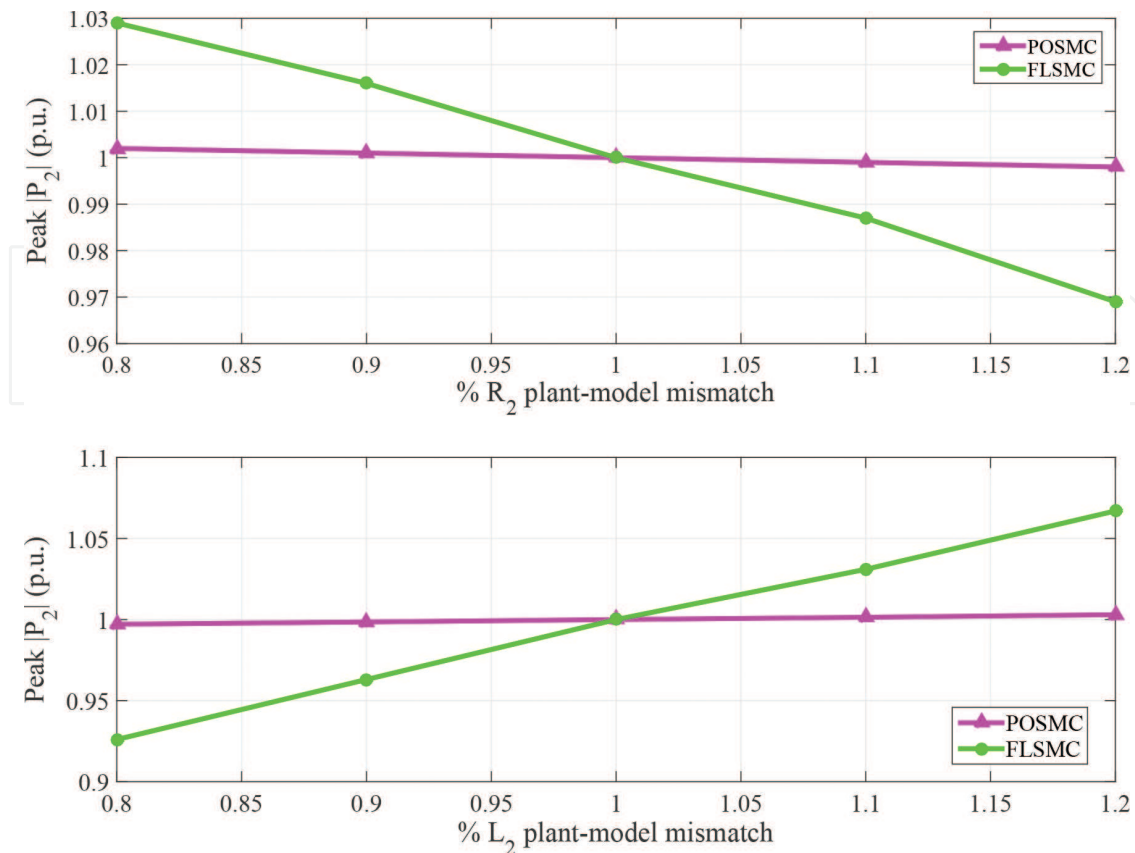
Figure 7. The peak active power $|P_2|$ (in p.u.) to a -120 A in the DC cable current i_L obtained at nominal grid voltage for plant-model mismatches in the range of 20% (one parameter changes and others keep constant).

while POSMC can effectively suppress such oscillation with the smallest fluctuation of DC voltage and reactive power.

(4) Case 4: System parameter uncertainties: When there is a fault in the transmission or distribution grid, the resistance and inductance values of the grid may change significantly. Several tests are performed for plant-model mismatches of R_2 and L_2 with $\pm 20\%$ uncertainties. All tests are undertaken under the nominal grid voltage and a corresponding -120 A in the DC cable current i_L at 0.1 s. The peak active power $|P_2|$ is recorded, which uses per unit (p.u.) value for a clear illustration of system robustness. It can be found from **Figure 7** that the peak active power $|P_2|$ controlled by POSMC is almost not affected, while FLSMC has a relatively large range of variation, i.e., around 3% to R_2 and 8% to L_2, respectively. Responses to mismatch of R_2 and L_2 changing at the same time are demonstrated in **Figure 8**. The magnitude of changes is around 10% under FLSMC and almost does not change under POSMC. This is because POSMC estimates all uncertainties and does not need an accurate system model, thus it has better robustness than that of FLSMC which requires accurate system parameters.

The integral of absolute error (IAE) indices of each approach calculated in different cases are tabulated in **Table 3**. Here, $\text{IAE}_{Q_1} = \int_0^T |Q_1 - Q_1^*|\mathrm{d}t$, $\text{IAE}_{V_{dc1}} = \int_0^T |V_{dc1} - V_{dc1}^*|\mathrm{d}t$, $\text{IAE}_{Q_2} = \int_0^T |Q_2 - Q_2^*|\mathrm{d}t$, and $\text{IAE}_{P_2} = \int_0^T |P_2 - P_2^*|\mathrm{d}t$. The simulation time $T = 3$ s. Note that POSMC has
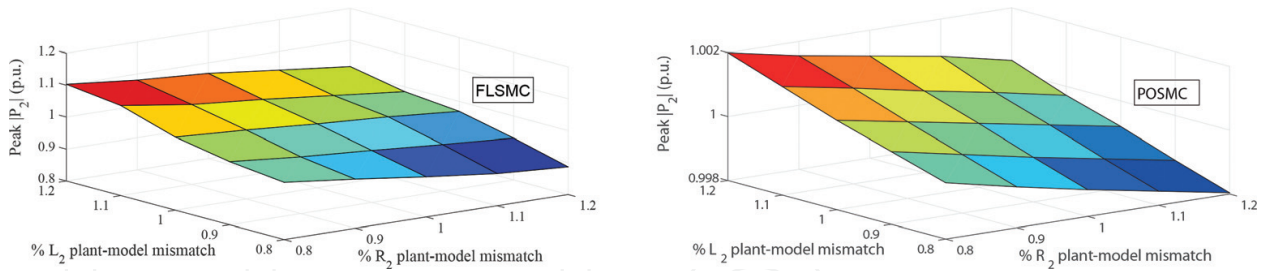
Figure 8. The peak active power $|P_2|$ (in p.u.) to a -120 A in the DC cable current i_L obtained at nominal grid voltage for plant-model mismatches in the range of 20% (different parameters may change at the same time).

| Method | Power tracking | | | |
Case				
	IAE_{Q_1}	$IAE_{V_{dc1}}$	IAE_{Q_2}	IAE_{P_2}
VC	3.83E-02	4.44E-03	2.13E-02	2.71E-02
FLSMC	2.19E-02	1.73E-03	2.23E-02	2.18E-02
POSMC	2.33E-02	2.00E-03	2.42E-02	2.33E-02
Method	Five-cycle LLLG fault		Weak AC grid connection	
Case				
	IAE_{Q_1}	$IAE_{V_{dc1}}$	IAE_{Q_1}	$IAE_{V_{dc1}}$
VC	2.62E-02	2.15E-03	4.53E-03	4.13E-03
FLSMC	1.13E-02	4.13E-03	4.08E-03	3.33E-03
POSMC	5.64E-03	1.38E-03	3.88E-04	6.78E-04

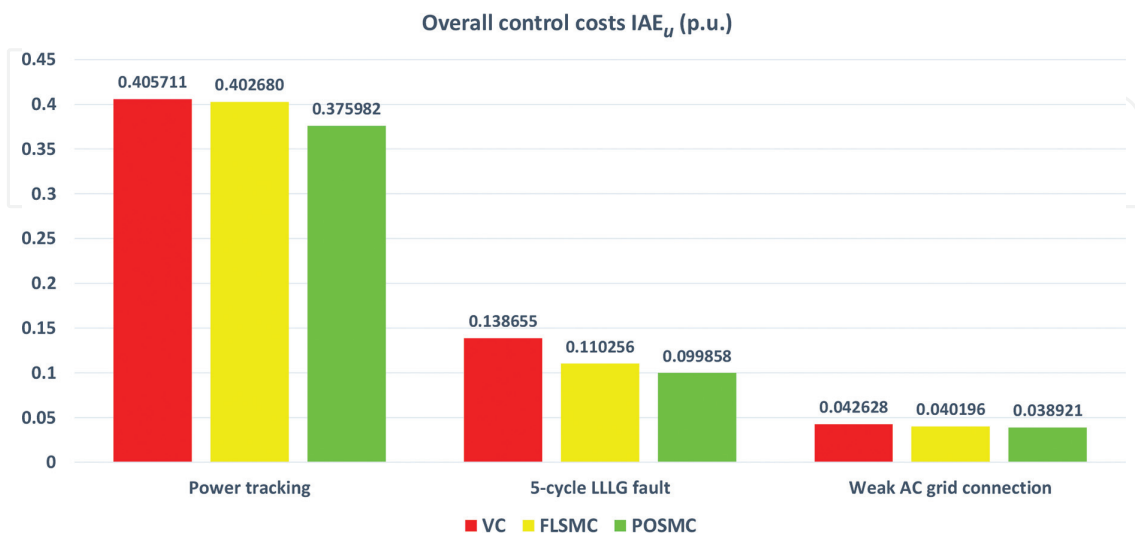**Table 3.** IAE indices (in p.u.) of different control schemes calculated in different cases.

Figure 9. Overall control costs IAE_u (in p.u.) obtained in different cases.

a little bit higher IAE than that of FLSMC in the power tracking due to the estimation error, while it can provide much better robustness in the case of 5-cycle LLLG fault and weak AC grid connection. In particular, its IAE_{Q_1} and $\text{IAE}_{V_{\text{dc1}}}$ are only 8.57 and 9.51% of those of VC, 16.42 and 20.36% of those of FLSMC with the weak AC grid connection. The overall control costs are illustrated in **Figure 9**, with $\text{IAE}_u = \int_0^T \left(|u_{\text{d1}}| + |u_{\text{q1}}| + |u_{\text{d2}}| + |u_{\text{q2}}| \right) \mathrm{d}t$. It is obvious that POSMC has the lowest control costs in all cases, which is resulted from the merits that the upper bound of perturbation is replaced by the smaller bound of its estimation error, thus an over-conservative control input can be avoided.

5. Hardware-in-the-loop test results

HIL test is an important and powerful technique used in the development and test of complex real-time embedded systems, which provides an effective platform by adding the complexity of the plant under control to the test platform. The complexity of the plant under control is included in test and development by adding a mathematical representation of all related dynamic systems.

A dSPACE simulator-based HIL test is used to validate the implementation feasibility of POSMC, which configuration and experiment platform are given by **Figures 10** and **11**, respectively. The rectifier controller (34) and inverter controller (41) are implemented on one dSPACE platform (DS1104 board) with a sampling frequency $f_c = 1\,\text{kHz}$, and the VSC-HVDC system is simulated on another dSPACE platform (DS1006 board) with the limit sampling frequency
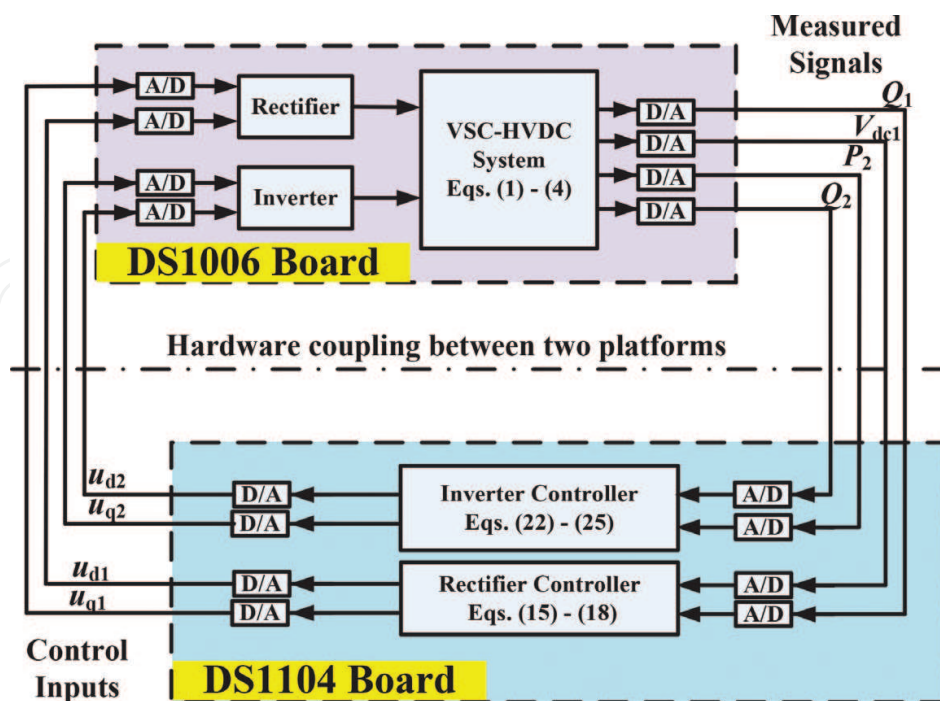

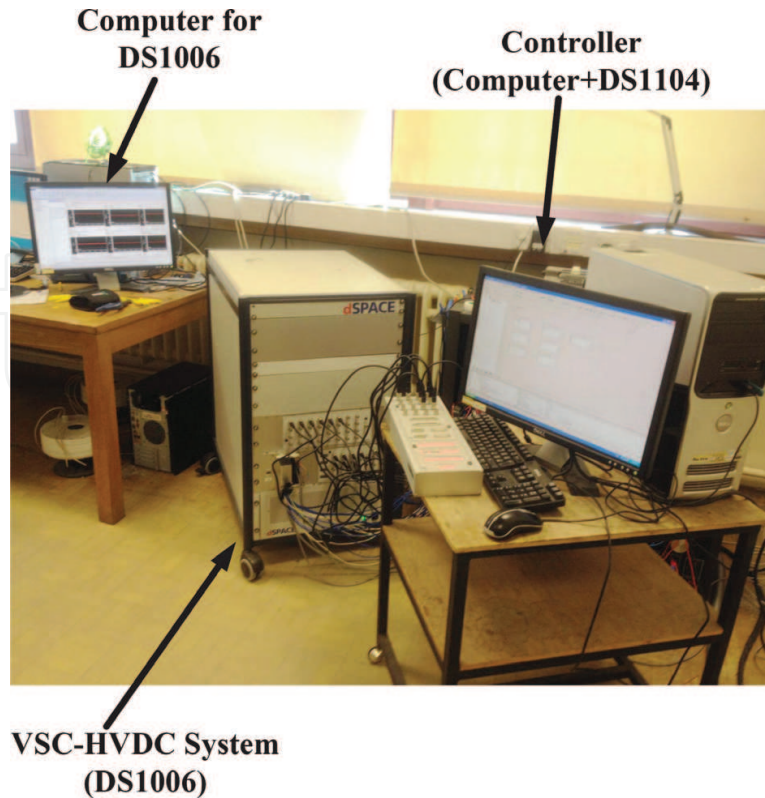**Figure 10.** The configuration of the HIL test.

Figure 11. The experiment platform of the HIL test.

$f_s = 50$ kHz to make HIL simulator as close to the real plant as possible. The measurements of the reactive power Q_1, DC voltage V_{dc1}, active power P_2, and reactive power Q_2 are obtained from the real-time simulation of the VSC-HVDC system on the DS1006 board, which are sent to two controllers implemented on the DS1104 board for the control inputs calculation.

It follows from [37] that an unexpected high-frequency oscillation in control inputs may emerge as the large observer poles would result in high gains, which lead to highly sensitive observer dynamics to the measurement disturbances in the HIL test. Note that this phenomenon does not exist in the simulation. One effective way to alleviate such malignant effect is to reduce the observer poles. Through trial-and-error, an observer pole in the range of $\lambda_{\alpha_r} \in [15, 25]$ and $\lambda_{\alpha'_r} = \lambda_{\alpha_i} = \lambda_{\alpha'_i} \in [3, 10]$ can avoid such oscillation but with almost similar transient responses, thus the reduced poles $\lambda_{\alpha_r} = 20$ and $\lambda_{\alpha'_r} = \lambda_{\alpha_i} = \lambda_{\alpha'_i} = 5$, with $b_{r10} = 50$, $b_{r20} = 5000$, $b_{i10} = 20$, and $b_{i20} = 20$, are chosen in the HIL test. Furthermore, a time delay $\tau = 3$ ms has been assumed in the corresponding simulation to consider the effect of the computational delay of the real-time controller.

(1) Case 1: Active and reactive power tracking: The reference of active and reactive power changes at $t = 0.4$ s, $t = 0.9$ s and restores to the original value at $t = 1.4$ s, while DC voltage is regulated at the rated value $V^*_{dc1} = 150$ kV. The system responses obtained under the HIL test and simulation are compared by **Figure 12**, which shows that the HIL test has almost the same results as that of the simulation.
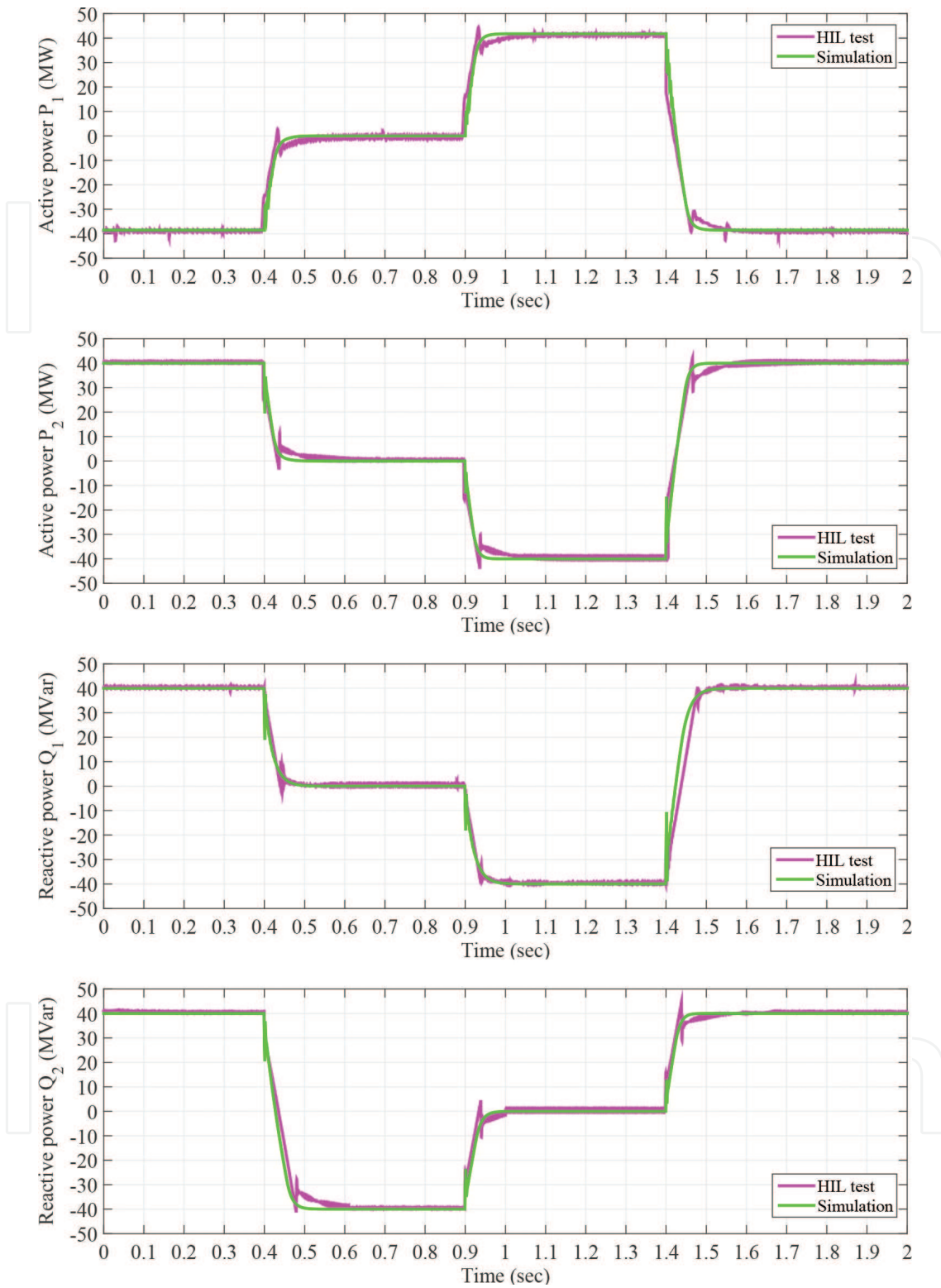
Figure 12. HIL test results of system responses obtained under the active and reactive power tracking.

(2) Case 2: 5-cycle line-line-line-ground (LLLG) fault at AC bus 1. A 5-cycle LLLG fault occurs at AC bus 1 when $t = 0.1$ s. **Figure 13** demonstrates that the system can be rapidly restored and the system responses obtained by the HIL test is similar to that of simulation.
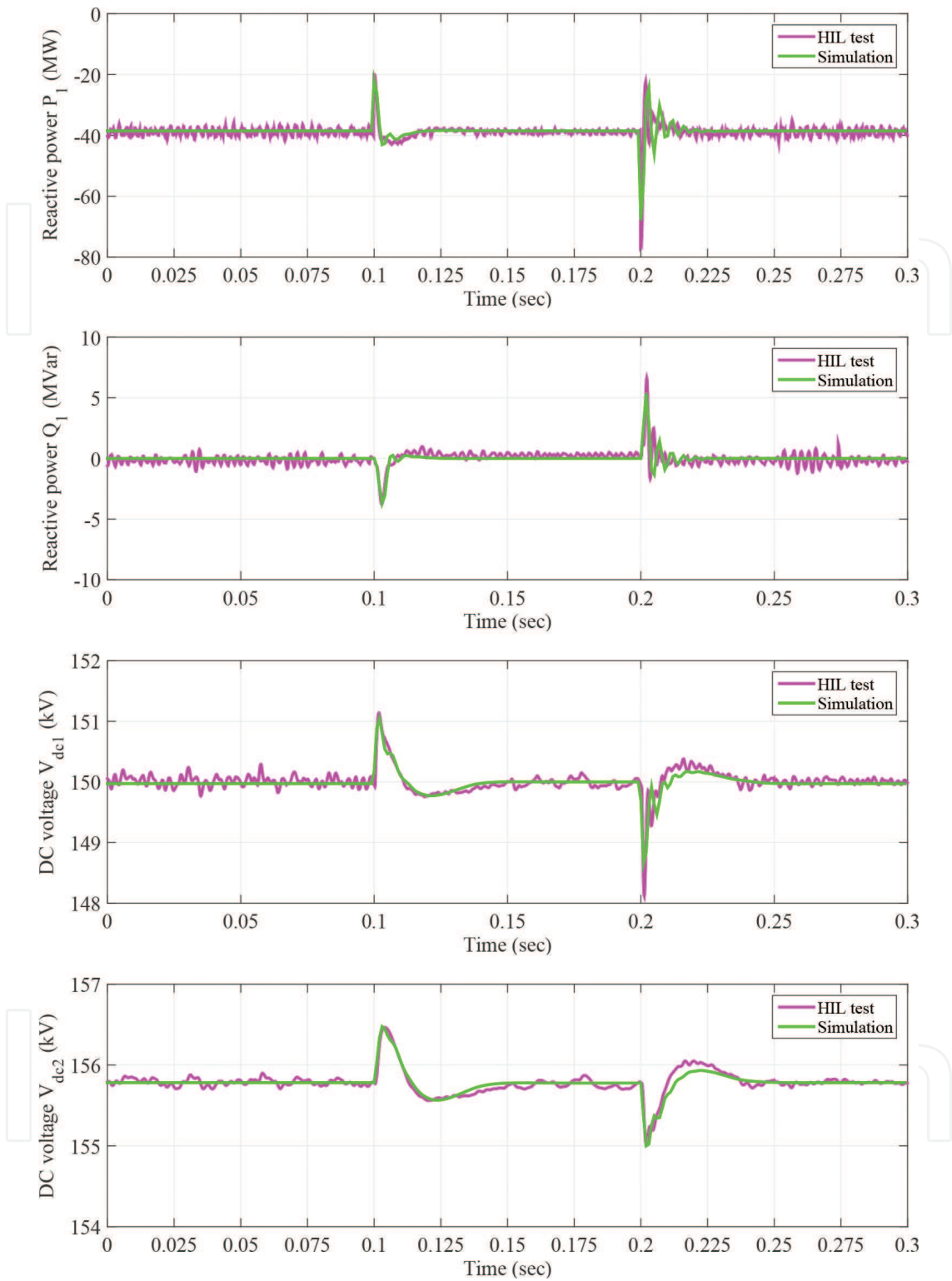
Figure 13. HIL test results of system responses obtained under the five-cycle LLLG fault at AC bus 1.

(3) Case 3: Weak AC grid connection: The same voltage variation $u_{s1} = 1 + 0.15 \sin{(0.2\pi t)}$ is applied between 0.87 and 2.45 s. It can be readily seen from **Figure 14** that the results of the HIL test and simulation match very well.
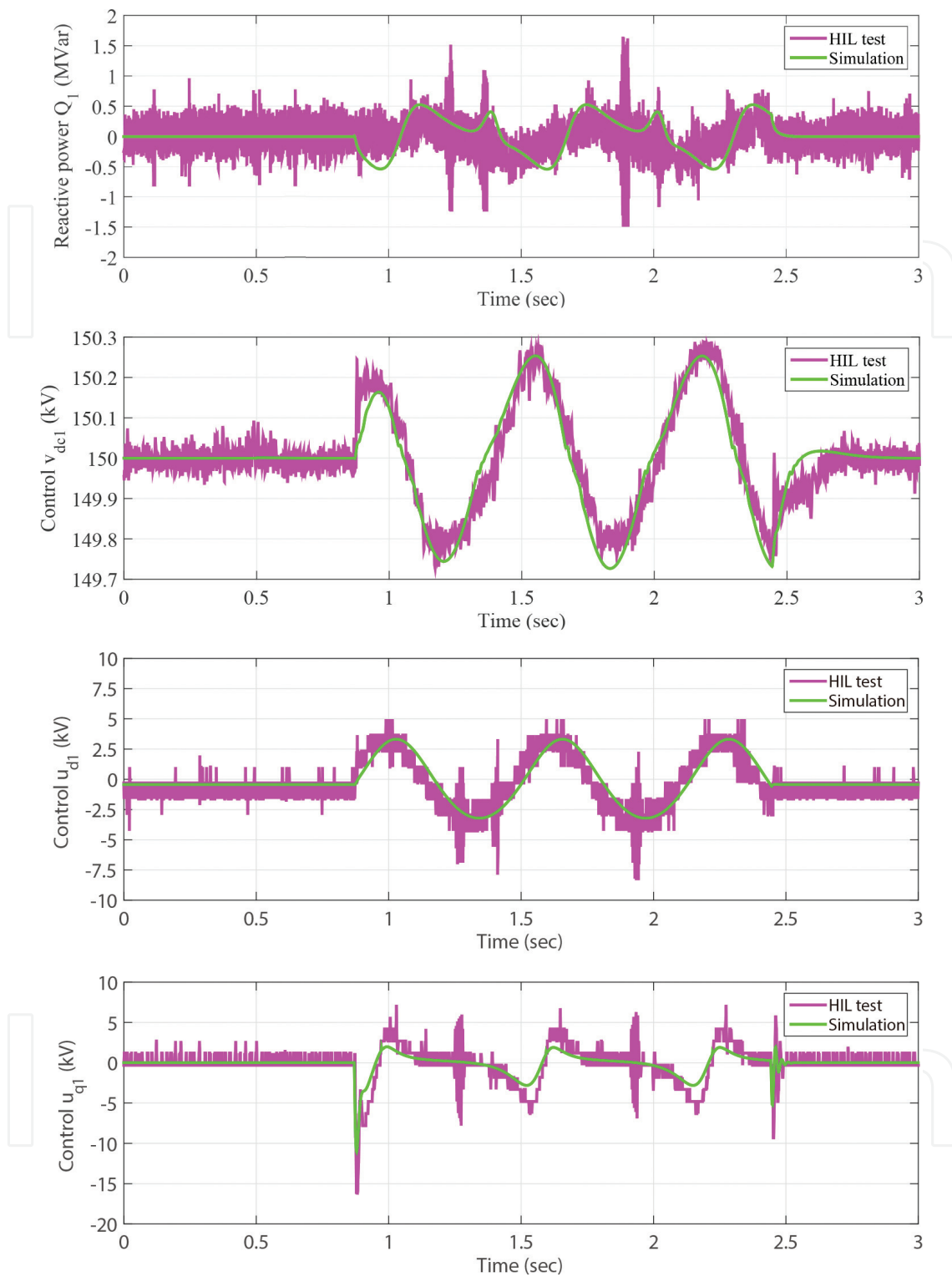
Figure 14. HIL test results of system responses obtained with the weak AC grid connection.

The difference of the obtained results between the HIL test and simulation is possibly due to the following two reasons:

- There exist measurement disturbances in the HIL test, which are, however, not taken into account in the simulation, a filter could be used to remove the measurement disturbances, thus the control performance can be improved.

- The sampling frequency of VSC-HVDC model and POSMC is the same in simulation ($f_s = f_c = 1$ kHz) as they are implemented in Matlab of the same computer. In contrast, the sampling frequency of VSC-HVDC model ($f_s = 50$ kHz) is significantly increased in the HIL test to make VSC-HVDC model as close to the real plant as possible. Note the sampling frequency of POSMC remains the same ($f_c = 1$ kHz) due to the sampling limit of the practical controller.

6. Conclusion

A POSMC scheme has been developed for the VSC-HVDC system to rapidly compensate the combinatorial effect of nonlinearities, parameter uncertainties, unmodeled dynamics, and time-varying external disturbances. As the upper bound of perturbation is replaced by the smaller bound of its estimation error, an over-conservative control input is avoided such that the tracking accuracy can be improved.

Four case studies have been undertaken to evaluate the control performance of the proposed approach, which verify that POSMC can maintain a consistent control performance with less power overshoot during the power reversal, restore the system rapidly after the AC fault, suppress the oscillation effectively when connected to a weak AC grid, and provide significant robustness in the presence of system parameter uncertainties. At last, a dSPACE-based HIL test has been carried out which validates the implementation feasibility of POSMC.

Acknowledgements

Author details

Bo Yang[1]*, Tao Yu[2], Hongchun Shu[1] and Pulin Cao[1]

*Address all correspondence to: yangbo_ac@outlook.com

1 Faculty of Electric Power Engineering, Kunming University of Science and Technology, Kunming, China

2 School of Electrical Engineering, South China University of Technology, Guangzhou, Guangdong, China

References

[1] Yang B, Yu T, Shu HC, Dong J, Jiang L. Robust sliding-mode control of wind energy conversion systems for optimal power extraction via nonlinear perturbation observers. Applied Energy. 2018;**210**:711-723

[2] Yang B, Hu YL, Huang HY, Shu HC, Yu T, Jiang L. Perturbation estimation based robust state feedback control for grid connected DFIG wind energy conversion system. International Journal of Hydrogen Energy. 2017;**42**(33):20994-21005

[3] Yang B, Sang YY, Shi K, Yao W, Jiang L, Yu T. Design and real-time implementation of perturbation observer based sliding-mode control for VSC-HVDC systems. Control Engineering Practice. 2016;**56**:13-26

[4] Yang B, Yu T, Zhang XS, Huang LN, Shu HC, Jiang L. Interactive teaching-learning optimizer for parameter tuning of VSC-HVDC systems with offshore wind farm integration. IET Generation Transmission and Distribution. 2018;**12**:678-687

[5] Yang B, Jiang L, Yao W, Wu QH. Perturbation observer based adaptive passive control for damping improvement of multi-terminal voltage source converter-based high voltage direct current systems. Transactions of the Institute of Measurement and Control. 2017; **39**(9):1409-1420

[6] Flourentzou N, Agelidis VG, Demetriades GD. VSC-based HVDC power transmission systems: An overview. IEEE Transactions on Power Electronics. 2009;**24**(3):592-602

[7] Hertema DV, Ghandhari M. Multi-terminal VSC HVDC for the European supergrid: Obstacles. Renewable and Sustainable Energy Reviews. 2010;**14**:3156-3163

[8] Zhang L, Harnefors L, Nee HP. Interconnection of two very weak AC systems by VSC-HVDC links using power-synchronization control. IEEE Transactions on Power Systems. 2011;**26**(1):344-355

[9] Zhang L, Harnefors L, Nee HP. Modeling and control of VSC-HVDC links connected to island systems. IEEE Transactions on Power Systems. 2011;**26**(2):783-793

[10] Haileselassie TM, Molinas M, Undeland T. Multi-terminal VSCHVDC system for integration of offshore wind farms and green electrification of platforms in the North Sea. Presented at the Nordic Workshop on Power and Industrial Electronics, Otakaari, Finland. 2008

[11] Li S, Haskew TA, Xu L. Control of HVDC light system using conventional and direct current vector control approaches. IEEE Transactions on Power Electronics. 2010;**25**(12): 3106-3118

[12] Ruan SY, Li GJ, Peng L, Sun YZ, Lie TT. A nonlinear control for enhancing HVDC light transmission system stability. International Journal of Electrical Power & Energy Systems. 2007;**27**:565-570

[13] Durrant M, Werner H, Abbott K. Synthesis of multi-objective controllers for a VSC HVDC terminal using LMIs. In: IEEE Conference of Decision and Control; 2004. pp. 4473-4478

[14] Ruan SY, Li GJ, Jiao XH, Sun YZ, Lie T. Adaptive control design for VSC-HVDC systems based on backstepping method. Electric Power Systems Research. 2007;**77**:559-565

[15] Lordelo A, Fazzolari H. On interval goal programming switching surface robust design for integral sliding mode control. Control Engineering Practice. 2014;**32**:136-146

[16] Huo W. Predictive variable structure control of nonholonomic chained systems. International Journal of Computer Mathematics-Computer Mathematics in Dynamics and Control. 2008;**85**(6):949-960

[17] Zong Q, Zhao ZS, Zhang J. Higher order sliding mode control with self-tuning law based on integral sliding mode. IET Control Theory and Applications. 2010;**4**(7):1282-1289

[18] Gokasan M, Bogosyan S, Goering DJ. Sliding mode based powertrain control for efficiency improvement in series hybrid-electric vehicles. IEEE Transactions on Power Electronics. 2006;**21**(3):779-790

[19] Kessal A, Rahmani L. Ga-optimized parameters of sliding-mode controller based on both output voltage and input current with an application in the PFC of AC/DC converters. IEEE Transactions on Power Electronics. 2014;**29**(6):3159-3165

[20] Lascu C, Boldea I, Blaabjerg F. Direct torque control of sensorless induction motor dirves: A sliding-mode approach. IEEE Transactions on Industrial Electronics. 2004;**40**(2):582-590

[21] Beltran B, Ahmedali T, Benbouzid MEH. Sliding mode power control of variable-speed wind energy conversion systems. Electric Machines & Drives Conference, 2007. IEMDC '07. IEEE International, Vol. 23, IEEE; pp. 551-558. 2008

[22] Moharana A, Dash PK. Input-output linearization and robust sliding-mode controller for the VSC-HVDC transmission link. IEEE Transactions on Power Delivery. 2010;**25**(3):1952-1961

[23] Edwards C, Spurgeon S. Sliding Mode Control: Theory and Applications. London, UK: CRC Press; 1998

[24] Johnson C. Accommodation of external disturbances in linear regulator and servomechanism problems. IEEE Transactions on Automatic Control. 1971;**16**(6):635-644

[25] Chen WH, Ballance DJ, Gawthrop PJ, O'Reilly J. A nonlinear disturbance observer for robotic manipulators. IEEE Transactions on Industrial Electronics. 2000;**27**(4):932-938

[26] She JH, Fang M, Ohyama Y, Hashimoto H, Wu M. Improving disturbance-rejection performance based on an equivalent-input disturbance approach. IEEE Transactions on Industrial Electronics. 2008;**55**(1):380-389

[27] Sun L, Li DH, Lee KY. Enhanced decentralized PI control for fluidized bed combustor via advanced disturbance observer. Control Engineering Practice. 2015;**42**:128-139

[28] Han JQ. From PID to active disturbance rejection control. IEEE Transactions on Industrial Electronics. 2009;**56**:900-906

[29] Sun L, Dong JY, Li DH, Lee KY. A practical multivariable control approach based on inverted decoupling and decentralized active disturbance rejection control. Industrial & Engineering Chemistry Research. 2016;**55**(7):2008-2019

[30] Guo BZ, Zhao ZL. On the convergence of an extended state observer for nonlinear systems with uncertainty. Systems and Control Letters. 2011;**60**(6):420-430

[31] Kwon SJ, Chung WK. Perturbation Compensator Based Robust Tracking Control and State Estimation of Mechanical Systems. New York: Springer; 2004

[32] Xia Y, Zhu Z, Fu M. Back-stepping sliding mode control for missile systems based on an extended state observer. IET Control Theory and Applications. 2011;**5**(1):93-102

[33] Yue M, Liu BY, An C, Sun XJ. Extended state observer-based adaptive hierarchical sliding mode control for longitudinal movement of a spherical robot. Nonlinear Dynamics. 2014; **78**:1233-1244

[34] Wang JX, Li SH, Yang J, Wu B, Li Q. Extended state observer-based sliding mode control for PWM-based DC-DC buck power converter systems with mismatched disturbances. IET Control Theory and Applications. 2015;**9**(4):579-586

[35] Jiang L, Wu QH, Wen JY. Nonlinear adaptive control via sliding-mode state and perturbation observer. IEE Proceedings - Control Theory and Applications. 2002;**149**(4): 269-277

[36] Liu Y, Wu QH, Zhou XX, Jiang L. Perturbation observer based multiloop control for the DFIGWT in multimachine power system. IEEE Transactions on Power Systems. 2014; **29**(6):2905-2915

[37] Yang B, Jiang L, Yao W, Wu QH. Perturbation estimation based coordinated adaptive passive control for multimachine power systems. Control Engineering Practice. 2015;**44**: 172-192

[38] Jovcic D. Phase locked loop system for FACTS. IEEE Transactions on Power Systems. 2003;**18**(3):1116-1124

[39] Jiang L.Nonlinear adaptive control and applications in power systems [PhD thesis]. University of Liverpool; 2001

[40] Hernandez J, Barbot JP. Sliding observer-based feedback control for flexible joints manipulator. Automatica. 1996;**32**(9):1243-1254

[41] Khalil HK. Nonlinear Systems. 3rd ed. New Jersey: Prentice Hall; 2002

[42] Slotine JJE, Li W. Applied Nonlinear Control. London: Prentice-Hall; 1991

[43] Geddada N, Mishra MK, Kumar MV. SRF based current controller using PI and HC regulators for DSTATCOM with SPWM switching. International Journal of Electrical Power & Energy Systems. 2015;**67**:87-100

[44] Baran ME, Mahajan NR. Overcurrent protection on voltage-source-converter-based multiterminal DC distribution systems. IEEE Transactions on Power Delivery. 2007;**22**:406-412